

Investigation of complex MHD activity by a combined use of various diagnostics

This content has been downloaded from IOPscience. Please scroll down to see the full text.

2003 Nucl. Fusion 43 1801

(<http://iopscience.iop.org/0029-5515/43/12/023>)

View [the table of contents for this issue](#), or go to the [journal homepage](#) for more

Download details:

IP Address: 200.0.233.51

This content was downloaded on 11/07/2017 at 14:11

Please note that [terms and conditions apply](#).

You may also be interested in:

[Stochastic sawtooth reconnection in ASDEX Upgrade](#)

V. Igochine, O. Dumbrajs, H. Zohm et al.

[Tearing mode formation induced by internal crash events at different N](#)

V. Igochine, I. Classen, M. Dunne et al.

[Identification of external kink modes in JET](#)

G.T.A. Huysmans, T.C. Hender and B. Alper

[MHD stability of \(2,1\) tearing mode in Tore Supra discharges](#)

P. Maget, H. Lütjens, G. Huysmans et al.

[MHD activity as seen in soft x-ray radiation](#)

M Bessenrodt-Weberpals, H J de Blank, M Maraschek et al.

[MHD phenomena in reversed shear discharges on ASDEX Upgrade](#)

S. Günter, S. Schade, M. Maraschek et al.

[MHD mode activity in the ASDEX Upgrade tokamak](#)

V. Igochine, O. Dumbrajs, D. Constantinescu et al.

[Investigation of 3D tungsten distributions in \(1,1\) kink modes induced by toroidal plasma rotation](#)

M Weiland, A Gude, V Igochine et al.

[Control of magnetic islands in the STOR-M tokamak using resonant helical fields](#)

S. Elgriw, D. Liu, T. Asai et al.

Investigation of complex MHD activity by a combined use of various diagnostics

V. Igochine, S. Günter, M. Maraschek and the ASDEX Upgrade Team

Max-Planck-Institut für Plasmaphysik, Euratom Association, Garching, Germany

E-mail: vgi@ipp.mpg.de, sig@ipp.mpg.de and mrm@ipp.mpg.de

Received 14 April 2003, accepted for publication 3 October 2003

Published 1 December 2003

Online at stacks.iop.org/NF/43/1801

Abstract

A new combined method for investigation of magnetohydrodynamic (MHD) activity in fusion experiments is proposed. The main advantages of this approach are the possibility of a direct comparison of theory predictions with experimental observations by the simultaneous use of several diagnostics. The method has been applied successfully to different types of instabilities in conventional and advanced tokamak scenarios in ASDEX Upgrade. As examples, double tearing mode as well as neoclassical tearing modes are considered. The combined use of different diagnostics allows an accurate determination of the mode's eigenfunction.

PACS numbers: 52.30.Cv, 52.35.Py, 52.55.Fa, 52.70.Ds, 52.70.Gw, 52.70.La

1. Introduction

Magnetohydrodynamic (MHD) instabilities play an important role in fusion experiments. They may lead to confinement degradation, to restriction in the operation regime or even to disruptions. These MHD instabilities may have a rather complex character, and a detailed analysis helps to find their driving forces and their influence on the plasma parameters. Such an analysis requires both a simultaneous use of all available diagnostics and comparison with theoretical predictions. This paper focuses on four diagnostics, and especially on their simultaneous use to gain detailed information about the observed MHD instabilities. These are: magnetic measurements (Mirnov coils), soft x-ray (SXR) cameras, electron cyclotron emission (ECE) and motional Stark effect (MSE).

As MHD instabilities cause magnetic perturbations varying in time, they can be registered and studied by measuring these field perturbations outside the plasma [1]. In ASDEX Upgrade the magnetic measurements consist of a set of 32 poloidal and ten toroidal Mirnov coils [2]. Using these coils, plasma perturbations can be detected at the plasma edge even if their amplitude is quite small. By measuring the time derivative of the perturbation of the poloidal magnetic field, \dot{B}_θ , at different poloidal and toroidal locations the structure of magnetic perturbations (m , poloidal number; n , toroidal mode number) can be determined as well as their amplitude and frequency. In the case of two modes with the same helicity being resonant on different radii, however, no information about the inner mode can be gained from magnetic measurements, as the magnetic perturbation is screened by the outer resonant surface.

The SXR radiation emitted by the plasma is a very good tool to study MHD activities in the plasma core [3]. ASDEX Upgrade is equipped with five pinhole SXR cameras with 124 chords [4]. These lines of sight cover the whole plasma volume. This diagnostic provides information about the poloidal mode number and the mode frequency and allows us to perform a tomography reconstruction [5, 6].

A set of radiometry diagnostics to register ECE is used to determine the electron temperature of the plasma along an ECE line of sight with very high temporal and spatial resolution [7]. Using fast ECE channels, the radial mode structure can be obtained from the time evolution of the temperature profile, as this is related to the displacement of magnetic field lines caused by the mode. The cut-off density limit, however, restricts the applicability of these diagnostics.

Equilibrium reconstruction based on the MSE diagnostic provides information on the location of the rational q values in the plasma [8]. This information is limited however by the relatively large error bars, especially in the plasma centre. The region of MSE measurements in ASDEX Upgrade is between $\rho_{\text{tor}} = 0.2$ and 0.8 .

Thus, the available diagnostics give different information about the plasma perturbations and cover different plasma regions. In addition to the experimental observations, much information about the nature of the MHD instabilities can be gained by comparison with theoretical prediction.

2. The MHD interpretation code

The MHD interpretation code (MHD-IC) simulates experimental observations related to a given plasma perturbation for

the diagnostics mentioned above, accounting for real plasma geometry and for measured plasma parameters.

The starting point of the simulations is the expected structure of an instability inside the plasma. The instability is characterized by its poloidal (m) and toroidal mode (n) numbers, the frequency of the mode rotation (ω) and the radial component of the shift of the magnetic field lines due to the MHD mode (ξ_0). The first three parameters are determined from the experiment, and perturbations may be written in the following form:

$$\xi = \xi_0(r) \cos(m\Theta + n\varphi - \omega t) \quad (1)$$

where Θ and φ are the poloidal and toroidal angles, respectively. The initial guess for the form of the radial component $\xi_0(r)$ results from numerical simulations performed using the XTOR code [9, 10], or from theoretical models. For practical reasons, not the eigenfunction itself but a parametrized form is used in the code, such that only the parameters have to be varied to adjust the eigenfunction to the measurements. As an example, for a single tearing mode the radial profile $\xi_0(r)$ of the perturbation from XTOR is parametrized by the functional form:

$$\xi_0(r, a, b, c, d, r_{\text{res}}) = \begin{cases} (r - r_{\text{res}})^b \exp\left(-\left(\frac{|r - r_{\text{res}}|}{a}\right)^c\right) & r < r_{\text{res}} \\ (r - r_{\text{res}})^b \exp\left(-\left(\frac{|r - r_{\text{res}}|}{a}\right)^c\right) d & r > r_{\text{res}} \end{cases} \quad (2)$$

where a corresponds to the island width (W), b determines the behaviour of the function inside the island, c describes the decay of the perturbation outside the island, d shows the relative amplitude of the two peaks and r_{res} is the position of the resonant surface. In figure 1 this function is plotted for the parameters $a = 0.06$, $b = 3$, $c = 1$, $d = 1$, $r_{\text{res}} = 0.5$

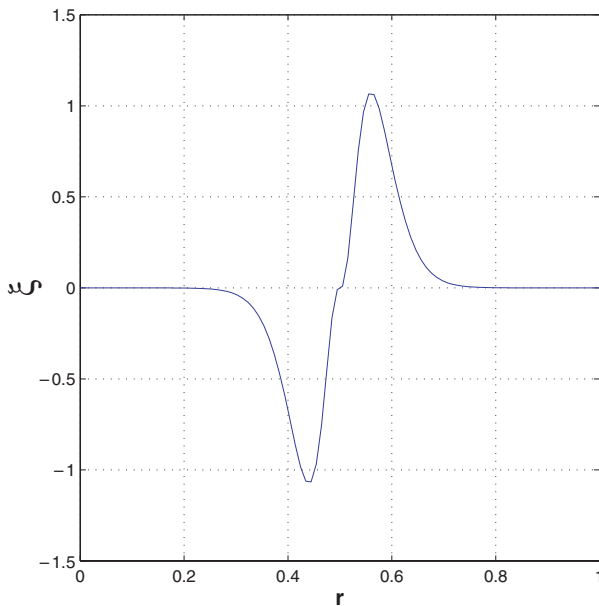


Figure 1. Parametrized function describing the magnetic perturbation due to a tearing mode.

and $W = 0.12$. When necessary, additional parameters were introduced to obtain a flexible analytical function representing the XTOR results. A process similar to that is used to get the initial values for the current perturbations, $J_{\text{pert}}(r)$. The width and the position of the island remain the same for both functions.

A scheme of how the code works is shown in figure 2. There are two branches of calculations inside the code. In the first part of the code, the perturbed magnetic field is calculated from the perturbation current, J_{pert} , at each point inside the ASDEX Upgrade vessel. It gives the possibility of comparing the phase and amplitude of the magnetic perturbation resulting from the calculation directly with the magnetic measurements.

In the second part, the emissivity along each line of sight, $I(N, r)$, is calculated and compared with the corresponding values measured by the SXR cameras. During this calculation the temperature profile along the ECE line of sight is calculated as well and compared with the experimental one.

For all calculations an equilibrium reconstruction including MSE data is used [8, 11]. The results of the MHD activity analysis regarding the rational surfaces are then applied to improve the equilibrium reconstruction. The whole analysis is then repeated in an iterative manner.

2.1. Magnetic measurements

Since the equilibrium current changes very slowly compared with the mode rotation velocity, the Mirnov coils in general detect only perturbation currents. Therefore, only the perturbation currents will be considered in the following.

Assuming toroidal coordinates (R, z, φ), where R is the major radius, z represents the vertical coordinate and φ corresponds to the toroidal angle, the perturbation field can be derived then from the perturbed poloidal flux, Ψ :

$$\vec{B}_p = \frac{1}{R} \nabla \Psi \times \vec{e}_\varphi \quad (3)$$

Substituting the magnetic field from (3) in Ampere's Law (4), and considering only the toroidal components of perturbation

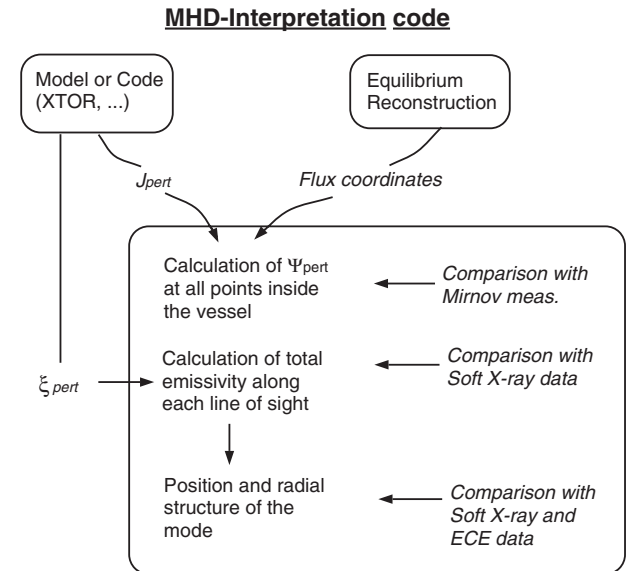


Figure 2. Structure of MHD-IC.

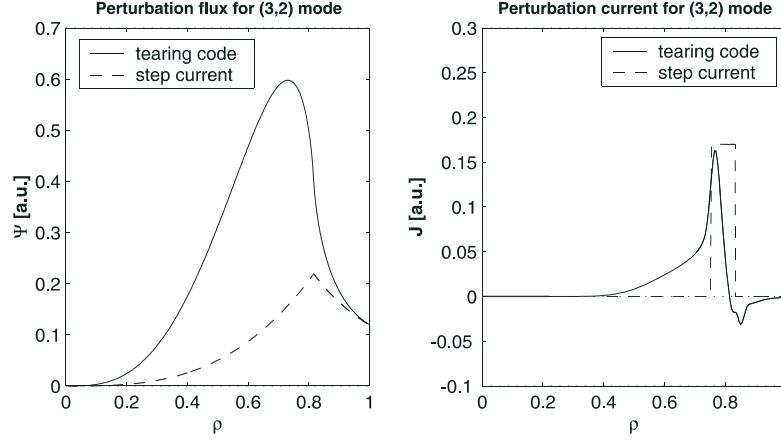


Figure 3. Perturbation fluxes and perturbation currents for a (3, 2) mode resulting from the tearing mode equation (—) and from a ‘step function’ assumption (---). One can see a significant difference between these two approaches ($r_{\text{res}} = 0.81$).

currents ($\partial_\varphi = 0$), Ampere’s Law (4) can be simplified to a two-dimensional elliptic differential equation (5), which is solved in real geometry¹. The vacuum vessel is assumed to be a perfect conductor.

$$\mu_0 J_\varphi = -\frac{1}{R} \Delta^* \Psi \quad (4)$$

$$-\left(\frac{\partial}{\partial R} \frac{1}{R} \frac{\partial}{\partial R} + \frac{\partial}{\partial z} \frac{1}{R} \frac{\partial}{\partial z} \right) \Psi(R, z) = \mu_0 J_\varphi(R, z) \quad (5)$$

By using only a constant current density [2], the radial profile of the perturbation current for a MHD mode has been assumed to be a constant over the region close to the corresponding rational surface. This approximation, however, is quite inaccurate. To demonstrate the difference between this assumption and the shape of a real perturbation current, the simple case of a tearing mode in cylindrical geometry will be considered. Assuming the perturbation flux at the plasma edge being the same, the perturbation fluxes using a step function for the current at the resonant surface and the solution of the tearing mode equation in cylindrical geometry have been evaluated. As shown in figure 3 the resulting fluxes and currents are quite different. It becomes obvious that for a given magnetic perturbation as measured by the Mirnov coils, the real plasma perturbations would be underestimated by only using a constant current density at the rational surface. For a more accurate treatment of the magnetic perturbation within the plasma, an arbitrary current profile is allowed in the MHD-IC. The detailed shape of the current perturbation, $J_{\text{pert}}(r)$, starts from a parametrized function approximating an XTOR code result as described before. For a single tearing mode the following parametrization is used:

$$J_{\text{pert}}(r) = \begin{cases} J_{\text{max}} \left(\frac{r - r_1}{r_2 - r_1} \right)^{\alpha_1} & r_1 < r < r_2 \\ (J_{\text{max}} - J_{\text{min}}) \frac{r - r_2}{r_2 - r_3} + J_{\text{max}} & r_2 \leq r \leq r_3 \\ J_{\text{min}} \left(1 - \frac{r - r_3}{r_4 - r_3} \right)^{\alpha_2} & r_3 < r < r_4 \end{cases} \quad (6)$$

where $r_2 = r_{\text{res}} - W/2$ and $r_3 = r_{\text{res}} + W/2$.

¹ The PLTMG solver for partial differential equations with the finite element grid method is used in the calculations [12].

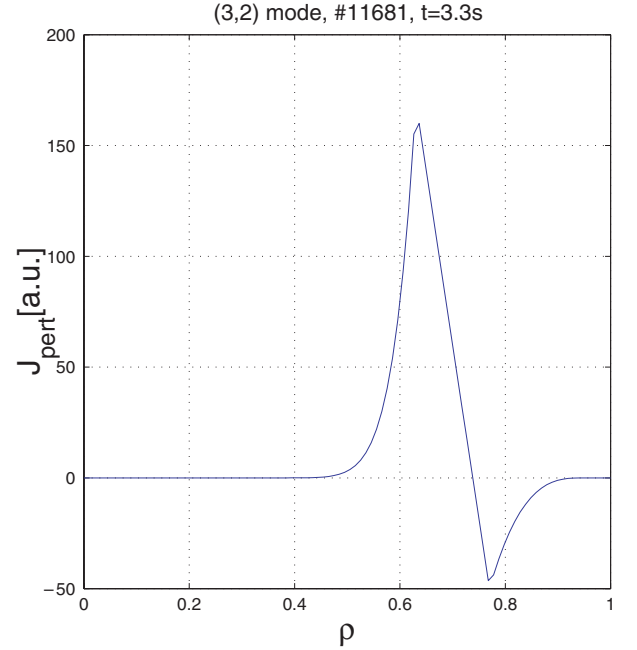


Figure 4. Perturbation current for (3, 2) mode, #11681, $t = 3.3$ s ($J_{\text{max}} = 170$, $J_{\text{min}} = -50$, $r_{\text{res}} = 0.7$, $W = 0.14$, $r_1 = 0.3$, $r_4 = 0.95$, $\alpha_1 = 8$ and $\alpha_2 = 3$).

As an example we consider a (3, 2) tearing mode. The position of the mode was found from ECE measurements. The shape of the perturbation current profile was varied to obtain the best agreement with magnetic measurements (see figure 4). The resulting perturbation flux due to the (3, 2) mode is shown in figure 5. A comparison of the calculated amplitude and phase with magnetic measurements is shown in figure 6. The resulting width of the islands from the magnetic measurements ($W = 7$ cm) is in good agreement with the corresponding ECE measurements.

2.2. SXR and ECE measurements

SXR and ECE signals give information about the behaviour of MHD modes directly from the plasma interior. Performing measurements along different lines of sight allows to determine

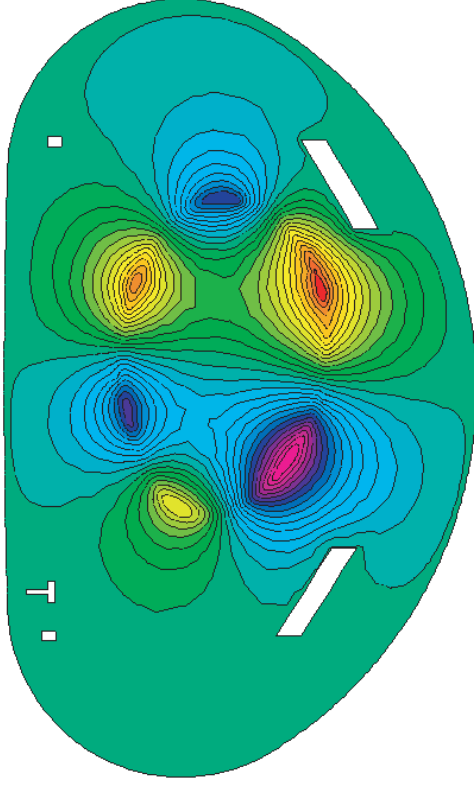


Figure 5. Calculation domain and perturbation flux for a (3, 2) tearing mode (#11681, $t = 3.3$ s).

the spatial behaviour and the amplitude of MHD activities inside the plasma.

The energy spectrum of SXR radiation consists of a continuum of free-free bremsstrahlung, free-bound recombination radiation and bound-bound line radiation (only minor contribution). For a Maxwellian velocity distribution and assuming hydrogen model for the impurity ions, the radiated power, $d\varepsilon$, per unit volume in the photon energy interval dE reads

$$\left(\frac{d\varepsilon}{dE}\right)_{\text{ff}} = \alpha n_e^2 Z_{\text{eff}} g_{\text{ff}}(T_e, E) \frac{\exp(-E/T_e)}{\sqrt{T_e}} \quad (7)$$

It depends strongly on the electron temperature, T_e [keV], the electron density, n_e [10^{13} cm^{-3}], and the impurity content, which determines the effective charge, $Z_{\text{eff}} = \sum_i n_i Z_i^2 / n_e$; $\alpha = 3 \times 10^{11}$ is a constant, and $g_{\text{ff}}(T_e, E)$ corresponds to the temperature-averaged Gaunt factor. The intensity results from integration over photon energy:

$$\varepsilon(r, \theta) = \int \varepsilon(E; r, \theta) f_{\text{camera}}(E) f_{\text{filter}}(E) dE \quad (8)$$

where $f_{\text{camera}}(E)$ contains the transmission coefficient of all elements inside the SXR cameras and $f_{\text{filter}}(E)$ represents beryllium foil filters.

Standard assumptions can be made to calculate the emissivity along a SXR line of sight. The line is divided into small pieces of length dL , and the plasma parameters are assumed to be uniform inside each piece. The resulting emissivity, $\varepsilon_{\text{total}}$, is then simply the sum over the emissivities

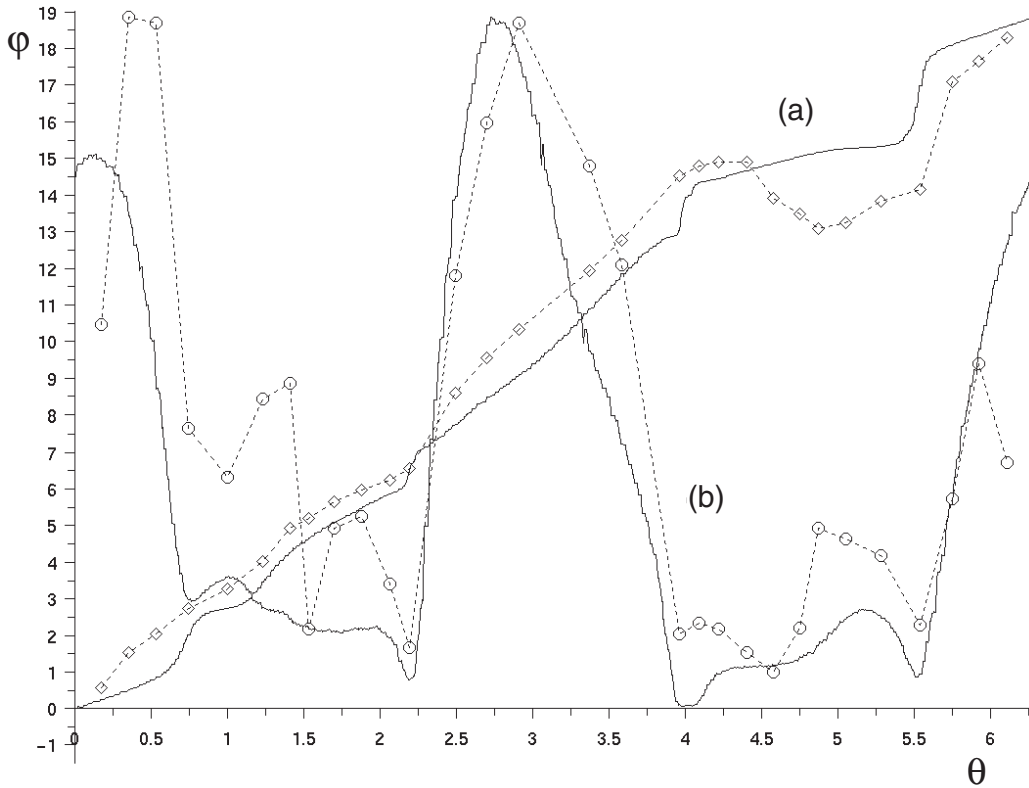


Figure 6. Phase (a) and amplitude (b) from calculation (—) compared with magnetic measurements (---), depending on the poloidal angle, θ , for the same discharge as in figures 4 and 5.

inside each element, multiplied by the element's length, dl :

$$\varepsilon_{\text{total}} = \sum_k \varepsilon_k dl \quad (9)$$

$$\varepsilon_k = G \frac{n_e^2}{\sqrt{T_e}} \sum_{i=1}^N f_{\text{sum}}(E_0 + i \Delta E) \times \exp\left(-\frac{E_0 + i \Delta E}{T_e}\right) \Delta E \quad (10)$$

In this equation, G represents a geometrical factor that describes the variation of the 'effective' width of a pinhole for different detectors inside one camera:

$$G = \frac{4\pi \Delta^2}{d_1 d_2 b_1 b_2 (\cos \alpha_i - (b_3/b_1) |\sin \alpha_i|)} \quad (11)$$

(d_1 , diode width; d_2 , diode length; b_1 , pinhole width; b_2 , pinhole length; b_3 , pinhole thickness; α_i , angle between the i th detector and the camera axis and Δ , focal length of pinhole camera). The transmission parameters of the system for different energies are collected in the coefficient $f_{\text{sum}}(E)$.

SXR signals $I(N, t)_{\text{calc}}$ (where N is line number and t represents time) are calculated using equations (9) and (10) for different phase angles of perturbations in order to simulate poloidal and toroidal rotation of the modes. As the MHD activities correspond solely to relative changes in the signal, an absolute calibration of the SXR cameras is not important here. From equation (7), it is obvious that the SXR signals are most sensitive to temperature perturbations. Changes of the Z_{eff} profile are not considered in the following, which is a good approximation for discharges without impurity puffing.

The structure of the SXR and the ECE part of the MHD-IC is shown in figure 7. In this part the displacement eigenfunction or the temperature perturbation is used as input parameters to describe the MHD activity. As actually the temperature perturbation is required, the following relation between the displacement and the temperature perturbation is used [13]:

$$\xi_{\text{pert}} = -\frac{T_{\text{pert}}}{\nabla T_{0,0}} \quad (12)$$

For the equilibrium quantities $T_{0,0}$, n_e and Z_{eff} , the measured values are used. The perturbations are added onto the equilibrium parameters, by using the equilibrium reconstruction (including MSE), transformed from the flux coordinates (ρ, θ) into the (R, z) plane. The resulting profiles

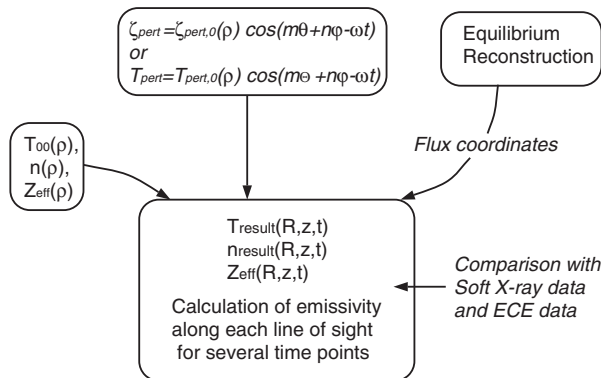


Figure 7. Scheme of the SXR part of MHD-IC.

$T(R, z, t)$, $n(R, z, t)$ and $Z_{\text{eff}}(R, z, t)$ are then used to simulate the SXR emissivity along a line of sight.

3. MHD activity analysis

3.1. Mirnov signals

An analysis of the MHD activity usually starts with identification of the dominant frequencies and determination of the mode numbers from magnetic measurements. After that, the phase and amplitude of the Mirnov signals are simulated and compared with experimental values as described in the previous section. The shape of the perturbation currents is varied to get the best possible agreement with experiment.

3.2. SXR signals

First information about the MHD activity can be found directly from the total SXR signal. As an example, in figure 8, the SXR signal of a discharge with a (2, 1) mode is given. The position of the camera lines of sight together with a (2, 1) mode structure is shown in figure 8(a). During the mode rotation, the SXR emissivity along the lines of sight $I(N, t)$ changes due to the temperature and density flattening inside the islands. The intensities $I(N, t)$ for two different positions of the island are shown in figure 8(b). The rotating mode changes the profile of the function $I(N, t)$ close to the resonant surface. Looking at a time series of the SXR intensity one finds a 'wave'-like structure in the mode position region, figure 8(c).

More detailed information can be gained if the perturbed part of the SXR signal is separated from the equilibrium background. One of the tools used in our calculations to do this is the fast Fourier transformation (FFT). Calculated and measured FFT amplitude and phase are compared with determine shape and position of the displacement eigenfunction of the observed MHD activity.

Another tool for our analysis is the singular value decomposition (SVD) [14, 15]. This algorithm gives the opportunity to separate the space- and time-dependent components of the perturbations from the total signal. Since the frequency of the mode rotation can easily be determined from experiment (Mirnov coils, SXR), most interesting for the analysis are the spatial components. The first spatial component corresponds to the unperturbed part of the signal, the unperturbed equilibrium. The second and the third components correspond to the strongest MHD activity [14]. The SVD for the calculated signal, $I(N, t)_{\text{calc}}$, and for the experimental signal, $I(N, t)_{\text{exp}}$, is performed in the code. By comparing the spatial SVD eigenvectors from theory and experiment, the best fit for the displacement eigenfunction is found.

The FFT and SVD techniques are flexible enough to obtain information about weak MHD activity even if this activity only slightly changes the total signal $I(N, t)_{\text{exp}}$. This is an advantage of the code compared with tomography reconstructions. The finite number of SXR detectors and errors in the absolute values of the emissivity lead to error bars in the radial direction of about $\Delta\rho \simeq 0.1\text{--}0.12$ (about 5–7 cm for ASDEX Upgrade) for the tomographic reconstruction [16]. On the other hand, by applying a combination of the FFT and the SVD techniques, and by using several SXR cameras simultaneously, the error bars can be reduced to

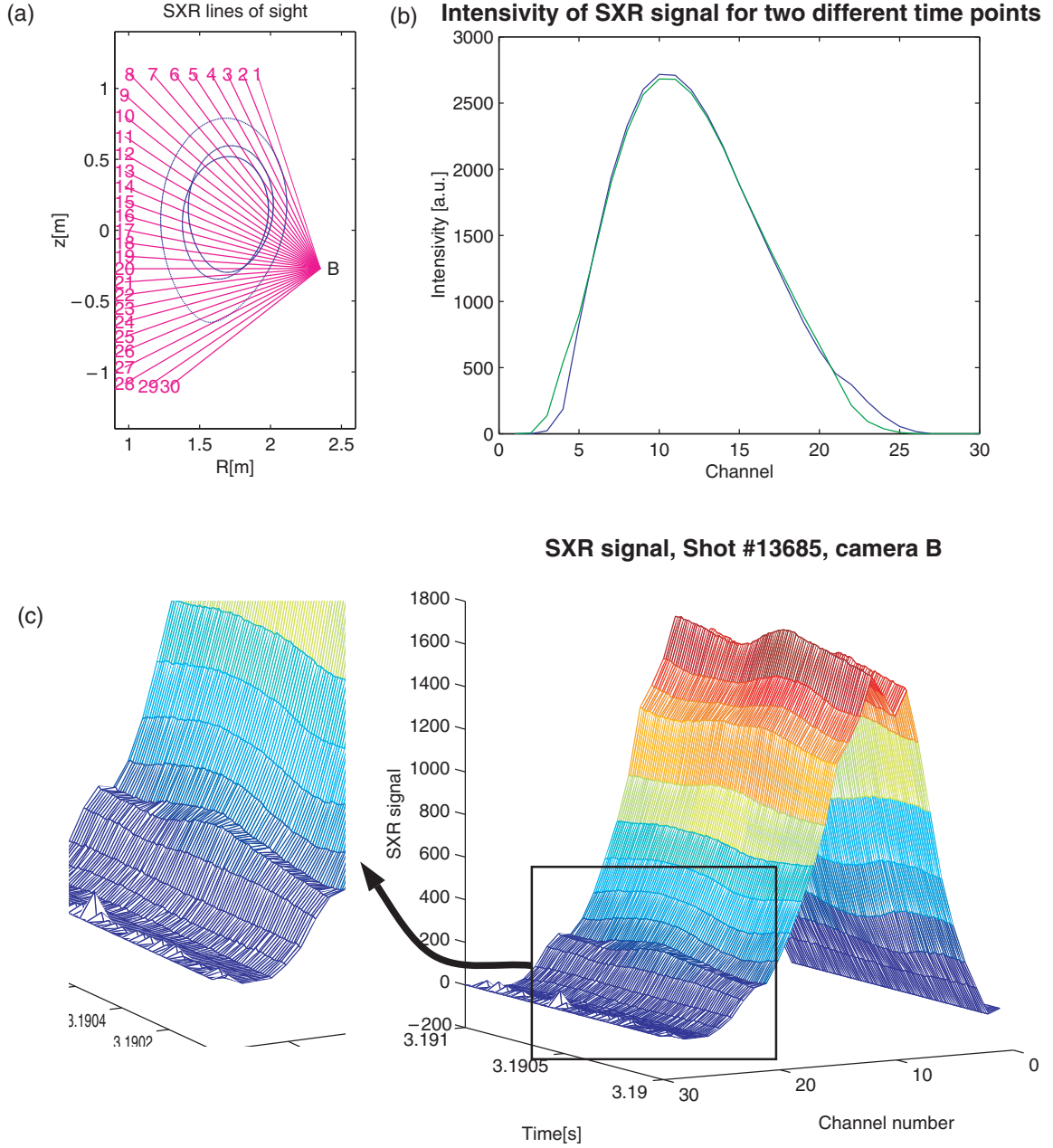


Figure 8. (a) Position of SXR lines of sight (B camera on ASDEX Upgrade) together with a sketch of (2, 1) magnetic islands. (b) Intensity for two different position of the islands. (c) Experimental SXR signal with ‘wave’-like structure.

$\Delta\rho \simeq 0.04\text{--}0.05$ (about 2–3 cm). One should note however that the FFT and SVD techniques cannot give any information about the absolute value of ξ ; a comparison of $I(N, t)_{\text{calc}}$ and $I(N, t)_{\text{exp}}$ would be required for that. As shown later, this comparison of $I(N, t)$ is not necessary if we obtain the absolute value of ξ from the ECE measurements.

3.3. ECE signals

The result of ECE measurements is the temperature profile, $T_e(R, z; t)_{\text{exp}}$, with high time resolution along the ECE line of sight. Using these fast ECE measurements it is possible to calculate the displacement eigenfunction directly from the

measured time-dependent temperature profile,

$$\xi_{\text{ece}} = \frac{T_e(t) - \langle T_e \rangle_t}{\nabla \langle T_e \rangle_t} \quad (13)$$

where $\langle \dots \rangle_t$ is time averaging over several periods of the poloidal mode rotation, and to compare it with ξ from the code input. In most cases it is difficult to obtain an absolute value of the displacement from SXR measurements, and this value can be found by fitting to the ECE result.

4. Analysis of complex MHD modes

In the following our analysis of the structure of MHD instabilities will be applied to two examples: the double tearing

mode (DTM) and a (3, 2) neoclassical tearing mode, toroidally coupled to a (2, 2) kink mode.

4.1. Double tearing mode

The advanced tokamak scenario is a promising option for tokamak operation as it allows improvement of the confinement or even steady state tokamak operation. Reversed shear profiles characteristic of these scenarios give rise to additional MHD phenomena like DTMs [17, 18]. This mode can appear if two rational surfaces with the same q values are close to each other, and thus two tearing modes on these surfaces can couple. Both modes have the same helicity, and thus the perturbation currents due to the inner mode are screened by the outer rational surface. Consequently, interpretation of the SXR signals and the ECE signals is the only way to find the radial structure of this mode.

As an example, we consider the mode activity in a reversed shear discharge of ASDEX Upgrade (#12224, $t = 0.7$ s), which will be shown to be a (2, 1) DTM. The magnetic measurements show a (2, 1) mode activity. The SXR signal from the 'B' camera is shown in figure 9. There is a 'wave'-like structure close to the central region of the plasma that is very similar to that shown in figure 8. This structure could correspond to an inner mode. A crude approximation of the position of an outer mode can also be found directly from figure 9 and from the MSE measurements.

For a detailed investigation of the instability, the fitting procedure for the eigenfunction was done. The starting form of the perturbation, ξ_{DTM} , results from the XTOR code and can

be parametrized by the following function:

$$\xi_{\text{DTM}} = \begin{cases} \xi_0(r, a, b, c_1, d_1) & r < r_1 \\ g\xi_0(r, a, b, c_2, d_3) - \xi_0(r, a, b, c_2, d_3) & r_1 \leq r \leq r_2 \\ -\xi_0(r, a, b, c_1, d_2) & r > r_2 \end{cases} \quad (14)$$

$$r_1 = r_{\text{res},1} + \frac{W}{2}, \quad r_2 = r_{\text{res},2} - \frac{W}{2} \quad (15)$$

By varying the shape of the function, the best fit for experimental values was found for $a = 0.0345$, $b = 1$, $c_1 = 5$, $c_2 = 0.75$, $d_1 = 2$, $d_2 = 0.5$, $d_3 = 1$, $g = 2$, $r_{\text{res},1} = 0.13$, $r_{\text{res},2} = 0.47$ and $W = 0.05$. Comparisons of the FFT amplitudes and the SVD components of this eigenfunction are shown in figures 10 and 11, respectively. The best fit for the eigenfunction ξ_{DTM} together with the q profiles is given in figure 12. From the shape of ξ_{DTM} , it becomes obvious that the investigated MHD activity is a (2, 1) DTM, showing a strong coupling between two rational surfaces. The position of the outer mode from our analysis is in good agreement with the outer $q = 2$ surface according to the equilibrium reconstruction. For the inner mode no information can be gained from the MSE measurements. Figure 12 shows two q profiles, which are both not in contradiction to the MSE measurements. Due to the reduced accuracy of the MSE measurements in the plasma centre, it is not clear whether an inner resonant surface exists at all.

ECE measurements are available over a large region of the plasma radius for this discharge (but do not include the inner mode). Thus, the radial displacement, ξ_{ece} , can be found from

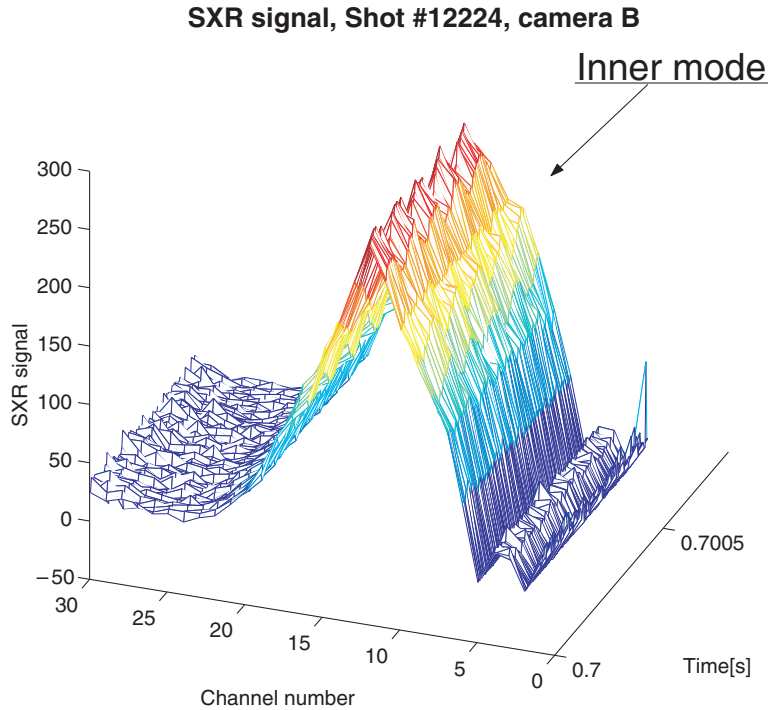


Figure 9. SXR signal from the B camera for the (2, 1) DTM (#12224, $t = 0.7$ s).

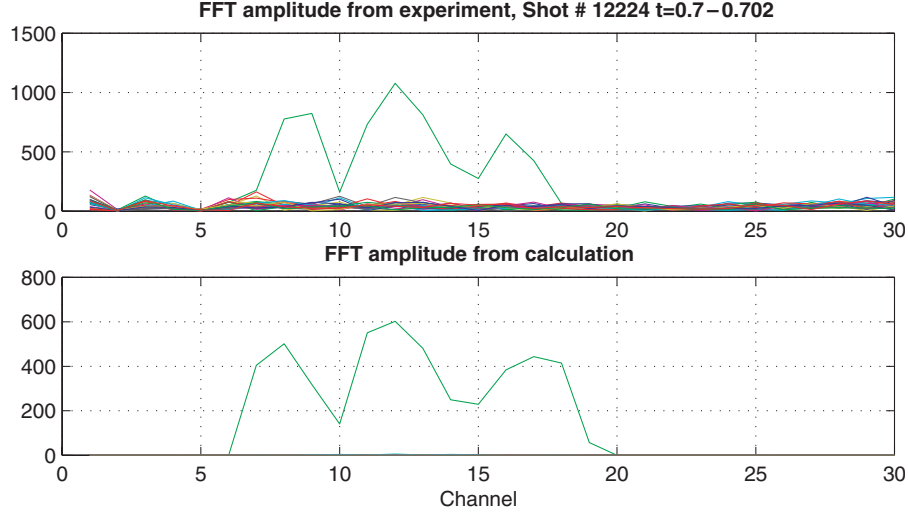


Figure 10. FFT amplitude for the same mode activity as in figure 9.

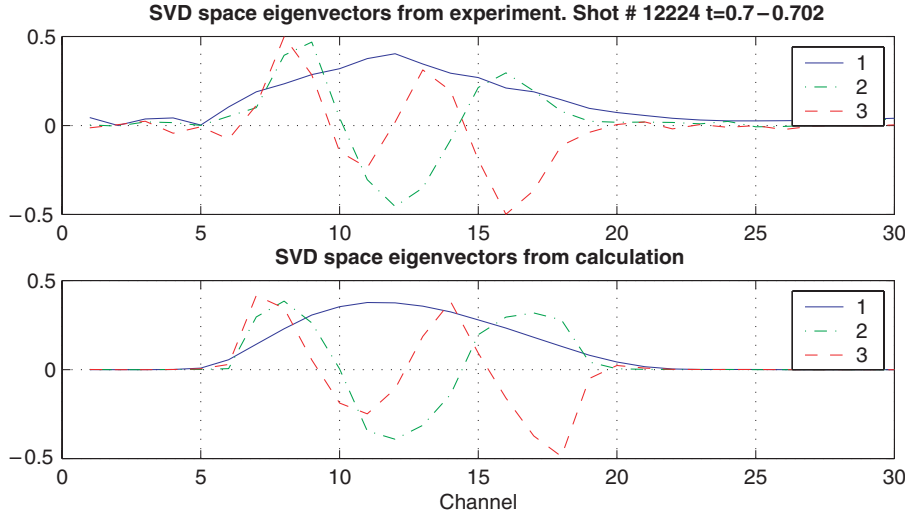


Figure 11. SVD eigenvectors for the mode of figures 9 and 10.

the temperature perturbation according to equation (13). These measurements verify a strong coupling between the modes. The shape of ξ_{ece} is in quite good agreement with the calculated ξ_{DTM} from the MHD-IC (figure 13). As was mentioned before, it is difficult to obtain an absolute value of the displacement from SXR measurements. This absolute value can be found by fitting ξ_{DTM} to ξ_{ece} .

The calculated SXR signals from the code are quite sensitive to the actual shape of the eigenfunction, and thus a good agreement between measurements and calculated signals can only be obtained for a good fit to the actual eigenfunction. To prove this, we choose an eigenfunction with only a weak coupling between the resonant surfaces (figure 14) and again perform the analysis for the same discharge (figures 15 and 16). It becomes obvious that for this profile of ξ the code results are in contradiction to the experiment.

It is also interesting to estimate the linear growth rate of the DTM from the derived eigenfunction. It was demonstrated in [19] that the relation from linear MHD approximation between perturbed flux and island width, $w^2 = 16(\psi/\psi_0'')$,

can be used for an island size of about 10% of the minor plasma radius. Assuming the perturbed flux outside the islands to be $\psi(r) = \xi(r)B_0(1 - q(r)n/m)$, and defining the equilibrium flux as $\psi_0(r) = B_0/R_0 \int_0^r (1/q(r) - n/m)r dr$, we can calculate the stability parameter Δ' for both modes in the DTM. In this approximation the growth of the DTM is described as a growth of two separate tearing modes [20, 21]. The stability parameters are different for both modes. At the same time, the product of stability parameter and resonant radius ($\Delta' r_{\text{res}}$) is constant for the both modes and determines the growth rate. Using the standard relation between $\Delta' r_{\text{res}}$ and the growth rate for tearing modes, we can find the growth rate. The resulting value for the growth rate is estimated to be $\gamma_{\text{DTM}} = 3.5(\pm 2.1) \times 10^3 \text{ s}^{-1}$. Slight variations of the displacement eigenfunction, $\xi(r)$, inside the error bars of the measurements have been used to estimate the error bars for this value. This result agrees quite well with that of a corresponding linear stability analysis using the CASTOR code [22] (based on an equilibrium reconstruction including MSE as well as density and temperature measurements for current and pressure

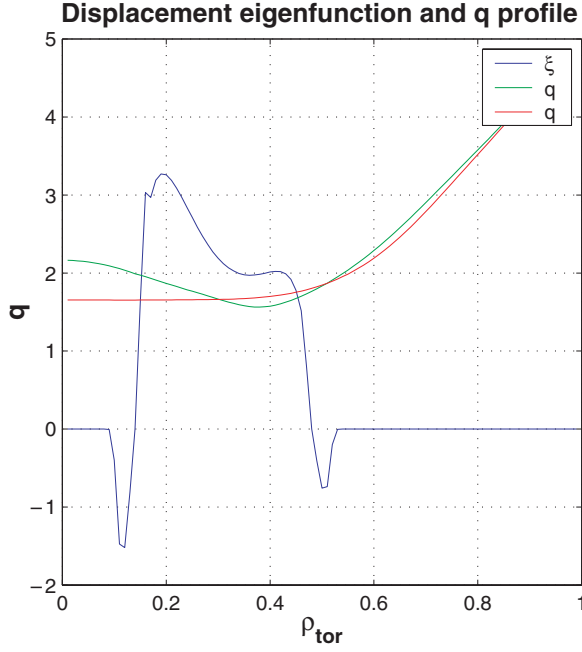


Figure 12. Displacement eigenfunction for the (2, 1) DTM and two q profiles resulting from the equilibrium reconstruction including the MSE measurements. Within the error bars, without considering the MHD activity, one cannot distinguish between the two profiles.

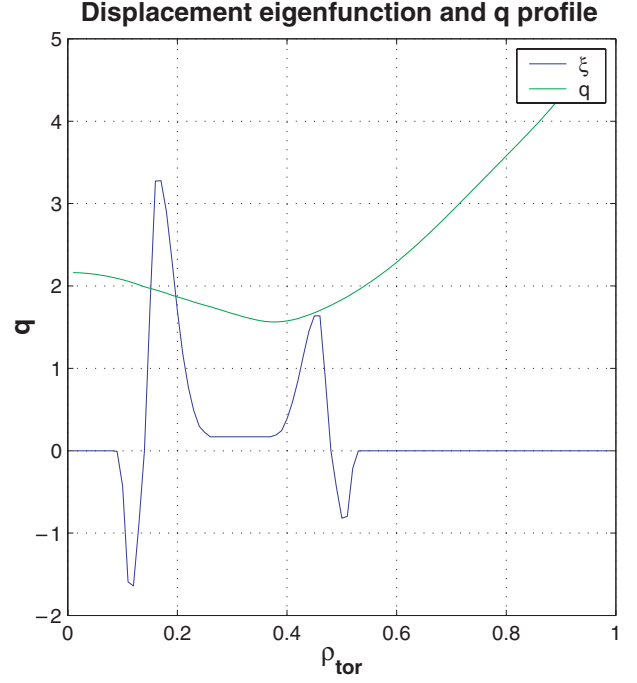


Figure 14. Displacement eigenfunction in case of weak coupling between the resonant surfaces together with the measured q profile (MSE).

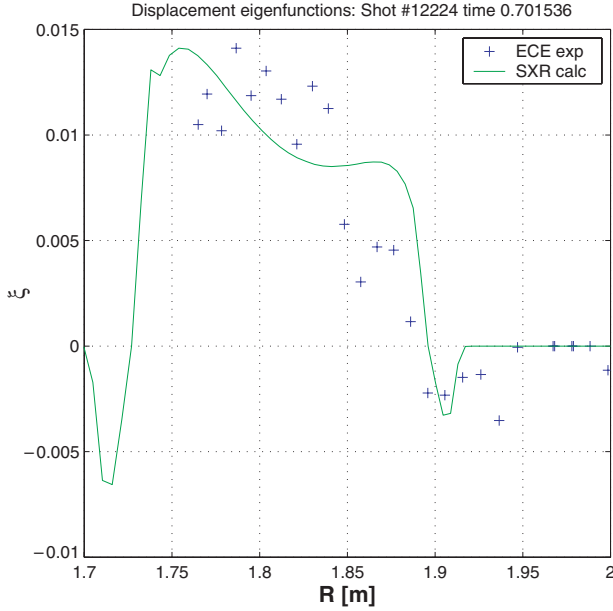


Figure 13. The displacement eigenfunction from ECE measurements together with the best fit according to equation (14) (shot #12224, $t = 0.7$ s).

profiles), leading to $\gamma = 3.0 \times 10^3 \text{ s}^{-1}$, and agrees quite well with the observed growth rate ($\gamma = 1.8 \times 10^3 \text{ s}^{-1}$) of the amplitude of the SXR signal and that of the magnetic perturbation. As the derivation of the growth rate from the measured eigenfunction strongly depends on its detailed shape and the q profile, its agreement with the actually observed growth rate of the mode within a factor of 2 can be considered as a very good result.

4.2. Toroidal coupling of (3, 2) tearing and (2, 2) ideal kink modes

In conventional tokamak scenarios neoclassical tearing modes are the most relevant MHD instabilities. In most cases the toroidal coupling to the $(m - 1)$ mode is quite strong [23]. We have investigated here the toroidal coupling between a (3, 2) and a (2, 2) mode. Magnetic probes detect in this case only the (3, 2) mode, which is closer to the probes and provides a strong signal. Thus, the investigation of the inner (2, 2) mode requires additional diagnostics.

The displacement eigenfunctions for both modes have been reconstructed using the MHD-IC (for the ASDEX Upgrade discharge #10198, $t = 3.03$ s). The phase jump of the ECE signals gives the position of the (3, 2) mode, but close to the plasma centre we have only a few points and cannot resolve the displacement eigenfunction. These measurements can only be used to estimate the amplitude of the perturbations, but not the detailed shape of the displacement, which was derived from the SXR diagnostic. As expected, a (3, 2) island coupled to a (2, 2) kink mode is found. The parametrization of the eigenfunction is done in the following way: for the (3, 2) tearing mode, equation (2) is applied. As an initial guess for the (2, 2) kink mode displacement, the following function has been used:

$$\xi_{(2,2)} = \begin{cases} \max(\xi_0(r, a, b, c, d)) & \text{if } r < r_{\text{res}} + \frac{W}{2} \\ \xi_0(r, a, b, c, d) & \text{if } r \geq r_{\text{res}} + \frac{W}{2} \end{cases}$$

where ξ_0 is also defined by equation (2). We assume in the calculations that the mode coupling is strong at the low-field side of the tokamak and the O-point position corresponds to the maximum (2, 2) eigenfunction.

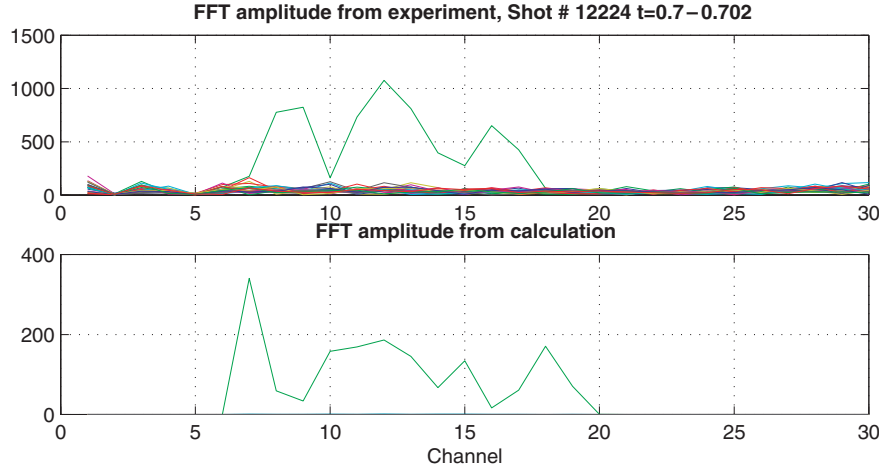


Figure 15. FFT amplitude calculated for the weak coupling case together with the FFT of the measured SXR signal.

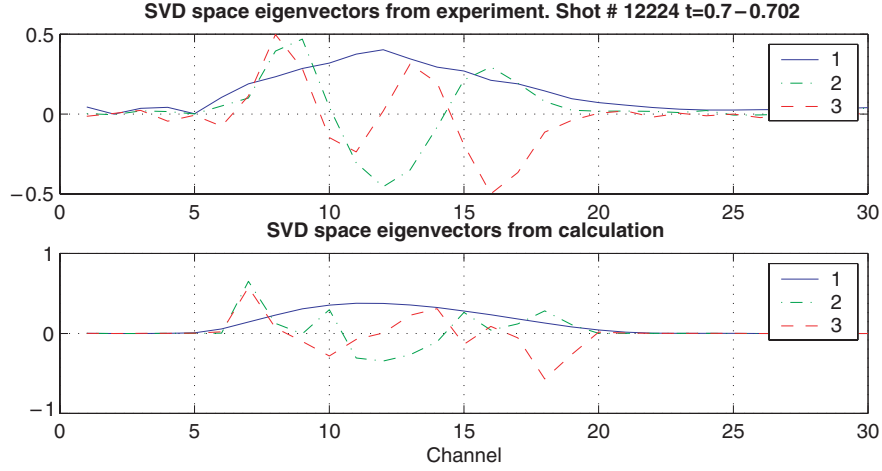


Figure 16. SVD eigenvectors for the weak coupling case together with the experimental ones.

An analysis of the SXR data is shown in figure 17. In this figure, the experimental FFT amplitude (figure 17(1b)) and the SVD eigenvectors (figure 17(1c)) are compared with different simulations by the MHD-IC. Varying the form of the displacement eigenfunctions, very good agreement with the experiment could be obtained for the following parameters: $a_{(3,2)} = 0.15$, $b_{(3,2)} = 1.0$, $c_{(3,2)} = 2.9$, $d_{(3,2)} = 0.5$, $r_{\text{res}(3,2)} = 0.56$, $a_{(2,2)} = 0.15$, $b_{(2,2)} = 1.0$, $c_{(2,2)} = 2.0$, $d_{(2,2)} = 1.0$, $r_{\text{res}(2,2)} = 0.23$ and $W = 0.184$. This case is shown in figures 17(2a–c). The displacement eigenfunctions in figure 17 are normalized to the ECE results and show the real amplitude of the displacement in metres. The next figures display the results of calculations for a smaller amplitude of the ideal kink mode (figures 17(3a–c)). In this case a reduced amplitude of the central peaks in FFT (figure 17(3b)) is obtained as these peaks correspond to the inner (2, 2) kink mode. The second SVD component, which mainly corresponds to the (2, 2) kink mode, is also in contradiction with the experimental one. In figures 17(4a–c) we take the amplitude of the (2, 2) mode to be the correct one (as in figure 17(2a)), but assume now that the (2, 2) kink mode has a resistive character. It is seen that even a small resistive part in the (2, 2) displacement strongly influences the results. This modification changes the

relative amplitude of the inner FFT peaks (figure 17(4b)) and destroys the agreement with the experiment for the second SVD component (figure 17(4c)). Our analysis of the inner mode demonstrates that the (2, 2) kink mode has an ideal character, and this ideal kink mode has approximately the same amplitude as the (3, 2) tearing mode. The resulting displacement eigenfunctions shown in figure 17(2a) give all the information about the spatial structure of the modes. It is worth noting that even special plasma tomographic methods, for instance differential rotation tomography [5], can only demonstrate the fact of mode coupling and give the position of the modes [16].

5. Summary and conclusions

Typical MHD instabilities can be studied by using standard techniques, but there are more complex MHD instabilities require special methods for their analysis. It was shown that a collection of all the available information about MHD instabilities resulting from different diagnostics increases the knowledge especially about the radial structure of the corresponding eigenfunction. A comparison with theoretical

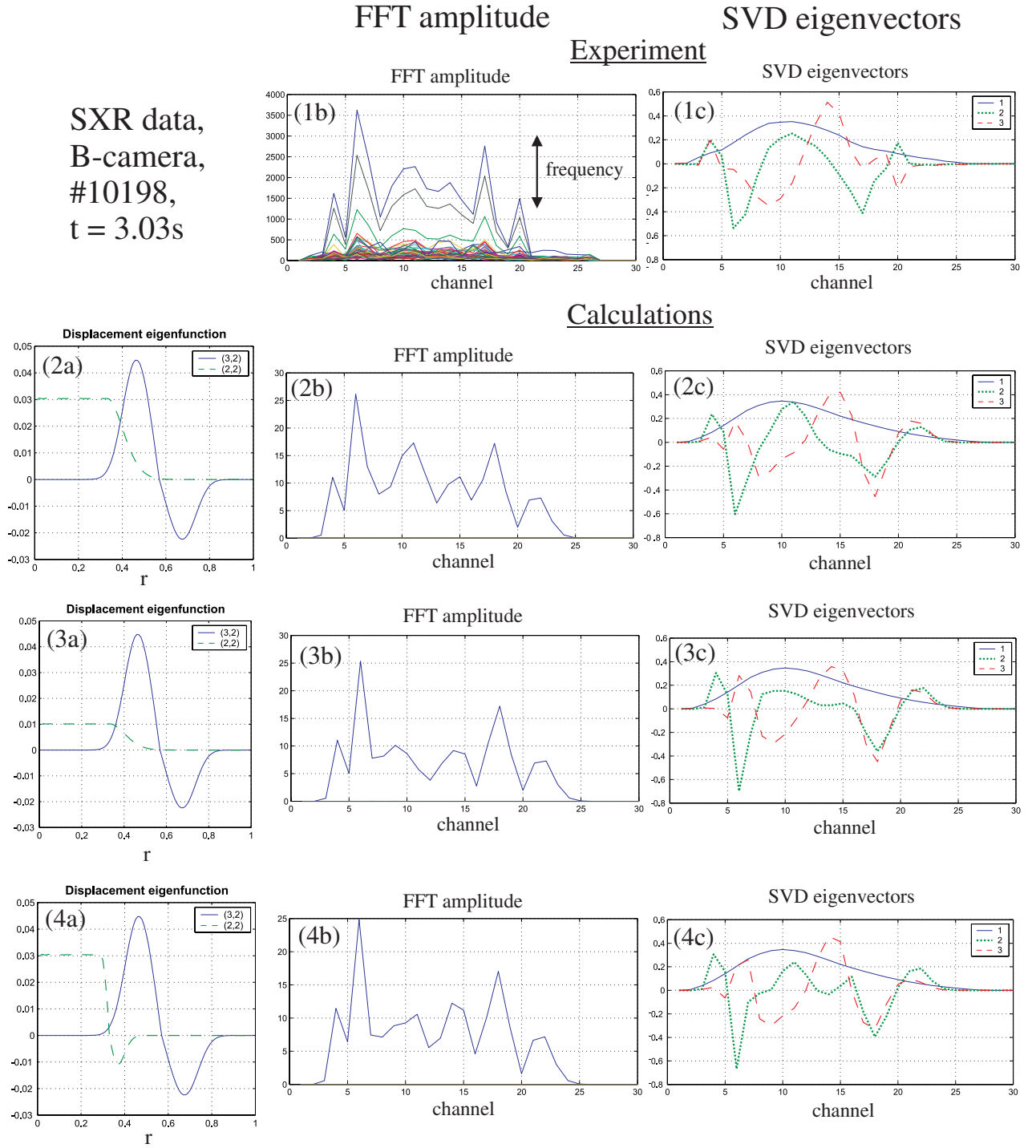


Figure 17. Analysis of the SXR data for toroidal coupling of (3, 2) neoclassical tearing mode and (2, 2) kink mode: experimental FFT amplitude (1b) and SVD eigenvectors (1c) are shown in the first line. The other pictures demonstrate results of MHD-IC calculations for different displacement eigenfunctions. Figures (2a–c) show the case with the best agreement with the experiment. Figures (3a–c) correspond to the small amplitude of the kink mode. Figures (4a–c) show the resistive kink mode case.

prediction by simulating the experimental signals for a given eigenfunction simplifies the identification of the observed MHD activity. In addition, the structure and the position of the observed MHD phenomena can be used for improving the equilibrium reconstruction especially in the plasma core, where the large error bars of the MSE measurements do not allow an accurate determination of the q profile.

We have applied the analysis developed to investigating the eigenfunction of a DTM as well as of a neoclassical tearing mode with strong toroidal coupling to the $m - 1$ sideband. The combination of different diagnostics (ECE, SXR) allowed a quite accurate determination of the eigenfunction. The analysis has been restricted to two main Fourier components here as this was sufficient for the considered examples. In

principle, however even more components could be included. Application of the method to other MHD modes is described in [21].

Acknowledgments

The authors would like to thank H. Lütjens for the possibility of using XTOR code to model MHD activity. The authors are grateful for help with MSE data analysis from J. Hobirk.

References

- [1] Mirnov S. and Semenov I. 1971 Investigation of instabilities of plasma column in ‘Tokamak-3’ device by correlation techniques *At. Energy (USSR)* **30**
- [2] Schittenhelm M., Zohm H. and ASDEX Upgrade Team 1997 Analysis of coupled MHD modes with Mirnov probes in ASDEX Upgrade *Nucl. Fusion* **37** 1255–70
- [3] Goeler S., Stodiek W. and Sauthoff N. 1974 *Phys. Rev. Lett.* **33** 1201
- [4] Bessenrodt-Weberpals M., Fuchs J., Sokoll M. and ASDEX Upgrade Team 1995 Soft x-ray diagnostics for ASDEX Upgrade *Report IPP 1/290*, Max-Planck-Institut für Plasmaphysik, Garching bei München
- [5] Sokoll M. 1997 MHD-instabilitäten in magnetisch eingeschlossen plasmen und ihre tomographische rekonstruktion im röntgenlicht. *Report IPP 1/309*, Max-Planck-Institut für Plasmaphysik, Garching bei München
- [6] Bessenrodt-Weberpals M., de Blank H., Maraschek M., McCarthy P., Sokoll M., Asmussen K. and ASDEX Upgrade Team 1996 MHD activity as seen in soft x-ray radiation *Plasma Phys. Control. Fusion* **38** 1543–59
- [7] Bornatici M., Cano R., de Barbieri O. and Engelmann F. 1983 *Nucl. Fusion* **23** 1153
- [8] McCarthy P., Wolf R.C., Hobirk J., Meister H. and Schneider W. 2000 Current profile identification on ASDEX Upgrade via motional Stark effect and the CLISTE interpretive equilibrium code *Abstr. 27th EPS* vol 24B, pp 440–3
- [9] Lütjens H., Bondeson A. and Roy A. 1992 Axisymmetric MHD equilibrium solver with bicubic hermite elements *Comput. Phys. Commun.* **69** 287–98
- [10] Lerbinger K. and Luciani J.F. 1991 A new semi-implicit method for MHD computations *J. Comput. Phys.* **97** 444–59
- [11] Schneider W., McCarthy P., Lackner K., Gruber O., Behler K., Martin P. and Merkel R. ASDEX Upgrade Team 2000 MHD equilibria reconstruction on distributed workstations *Fusion Eng. Des.* **48** 127–34
- [12] Bank R. 1990 *PLTMG: A Software Package for Solving Elliptic Partial Differential Equation* (Philadelphia: Society for Industrial and Applied Mathematics)
- [13] Fitzpatrick R. 1995 Helical temperature perturbations associated with tearing modes in tokamak plasmas *Phys. Plasmas* **2** 825–38
- [14] Schaback R. and Werner H. 1992 *Numerische Mathematik* (Berlin: Springer)
- [15] Dongarra J., Bunch J., Moler C. and Stewart G. 1979 *LINPACK Users’ Guide* (Philadelphia: SIAM)
- [16] Sokoll M. 1997 Interpretation and tomography of SXR data with the codes VISO and DIRO *Report IPP 1/310*, Max-Planck-Institut für Plasmaphysik, Garching bei München
- [17] Günter S., Schade S., Maraschek M., Pinches S., Strumberger E., Wolf R., Yu Q. and ASDEX Upgrade Team 2000 MHD phenomena in reversed shear discharges on asdex upgrade *Nucl. Fusion* **40** 1541–8
- [18] Günter S., Gude A., Hobirk J., Maraschek M., Saarlema S., Schade S., Wolf R. and ASDEX Upgrade Team 2001 MHD phenomena in advanced scenarios on ASDEX Upgrade and the influence of localized electron heating and current drive *Nucl. Fusion* **41** 1283–90
- [19] Fredrickson E., Bell M. and Synakowski E. 2000 Nonlinear evolution of double tearing modes in tokamaks *Phys. Plasmas* **7** 4112
- [20] Pritchett P.L., Lee Y.C. and Drake J.F. 1980 Linear analysis of the double-tearing mode *Phys. Fluids* **23** 1368–74
- [21] Igochine V. 2002 Investigation of MHD instabilities in conventional and advanced scenarios on ASDEX upgrade *Report IPP 5/101*, Max-Planck-Institut für Plasmaphysik, Garching bei München
- [22] Kerner W., Goedbloed J., Huysmans G., Poedts S. and Schwarz E. 1998 CASTOR: normal-mode analysis of resistive MHD plasmas *J. Comp. Phys.* **142** 271–303
- [23] Sesnic S., Günter S., Gude A., Maraschek M. and the ASDEX Upgrade Team 2000 Interaction of fast particles with neoclassical tearing modes *Phys. Plasmas* **7** 935–9